BNL-222732-2022-JAAM

Intercalation-Activated Layered MoO3 Nanobelts as Biodegradable Nanozymes for Tumor-Specific Photo-Enhanced Catalytic Therapy

Z. Zhou, L. Ma

To be published in "ANGEWANDTE CHEMIE-INTERNATIONAL EDITION"

January 2022

Photon Sciences

Brookhaven National Laboratory

U.S. Department of Energy

USDOE Office of Science (SC), Basic Energy Sciences (BES) (SC-22)

DISCLAIMER

RESEARCH ARTICLE WILEY-VCH

Intercalation-Activated Layered MoO_3 Nanobelts as Biodegradable Nanozymes for Tumor-Specific Photo-Enhanced Catalytic Therapy

Zhan Zhou,[1,10,†] Yanlong Wang,[2,7,†] Feng Peng,[3,†] Fanqi Meng,[4,†] Jiajia Zha,[5] Lu Ma,[6] Yonghua Du,[6] Na Peng,[7] Lufang Ma,[1] Qinghua Zhang,[4,8] Lin Gu,[4,8,*] Wenyan Yin,[2,*] Zhanjun Gu,[2,*] and Chaoliang Tan[5,9,*]

[1] Dr. Z. Zhou and Prof. L. Ma
College of Chemistry and Chemical Engineering, Henan Key Laboratory of Function-Oriented Porous Materials, Luoyang Normal University, Luoyang, 471934, PR China
[2] Y. Wang, Prof. W. Yin and Prof. Z. Gu
CAS Key Laboratory for Biomedical Effects of Nanomaterials and Nanosafety, Institute of High Energy Physics, Chinese Academy of Sciences, Beijing 100049, PR China
E-mail: yinwy@ihep.ac.cn (W. Yin); zjgu@ihep.ac.cn (Z. Gu)
[3] Prof. P. Feng
College of Physics and Electronic Information & Henan Key Laboratory of Electromagnetic Transformation and Detection, Luoyang Normal University, 471934, Luoyang, PR China
[4] F. Meng, Prof. Q. Zhang and Prof. L. Gu
Beijing National Laboratory for Condensed Matter Physics, Institute of Physics, Chinese Academy of Sciences, Beijing 100190, PR China
E-mail: l.gu@iphy.ac.cn (L. Gu)
[5] J. Zha and Prof. C. Tan
Department of Electrical Engineering, City University of Hong Kong, 83 Tat Chee Avenue, Kowloon, Hong Kong, PR China
E-mail: chaoltan@cityu.edu.hk (C. Tan)
[6] Dr. L. Ma and Dr. Y. Du
National Synchrotron Light Source II, Brookhaven National Laboratory Upton, Upton, NY, 11973 USA
[7] Y. Wang and Prof. N. Peng
Key Laboratory of Coal Conversion and New Carbon Materials of Hubei Province, School of Chemistry and Chemical Engineering, Wuhan University of Science and Technology, Wuhan, Hubei 430081, PR China
[8] Prof. Q. Zhang and Prof. L. Gu
School of Physical Sciences, University of Chinese Academy of Sciences, Beijing 100049, PR China
[9] Prof. C. Tan
Shenzhen Research Institute, City University of Hong Kong, Shenzhen, 518057 PR China
Institution
[10] Dr. Z. Zhou
People's Hospital of Zhengzhou University, Henan Provincial People's Hospital, Zhengzhou 450003, PR China

†These authors contribute equally to this work

Supporting information for this article, including the chemicals, instrumentation, synthesis and characterization (PDF), can be found under http://dx.doi.org/10.1002/anie.xxxxxxxxx.

Abstract: The existence of natural van der Waals gaps in layered materials allows them to be easily intercalated with varying guest species, offering an appealing strategy to optimize their physicochemical properties and application performance. Herein, we report the activation of layered MoO_3 nanobelts *via* aqueous intercalation as an efficient biodegradable nanozyme for tumor-specific photo-enhanced catalytic therapy. The long MoO_3 nanobelts are grinded and then intercalated with Na^+ and H_2O to obtain the short Na^+/H_2O co-intercalated MoO_3 nanobelts (NH-MoO_3). In contrast to the inert MoO_3 nanobelts, the NH-MoO_3 nanobelts exhibit excellent enzyme-mimicking catalytic activity for generation of reactive oxygen species, which can be further enhanced by the photothermal effect under a 1064 nm laser irradiation. Thus, after bovine serum albumin modification, the NH-MoO_3 nanobelts can efficiently kill cancer cells *in vitro* and eliminate tumors *in vivo* facilitating with 1064 nm laser irradiation.

Introduction

Layered materials are a class of functional materials with highly anisotropic bonding, in which each layer is strongly bonded *via* covalent bonding and adjacent layers are only weakly bonded *via* van der Waals interactions.[1-3] One of the unique advantages for layered materials is the existence of natural van der Waals gaps, allowing them to be easily intercalated with varying guest species, such as cations, anions, organic molecules and conductive polymers.[4-6] By taking this advantage, intercalation has been developed as one of the most appealing strategies to tune/optimize the physical, chemical and electronic properties of layered materials and/or boost their performance in various promising applications.[7-9] For example, the organic cation intercalation has been proposed as a fascinating approach to remarkably boost the thermoelectric and electronic device performance of layered TiS_2 and black phosphorus, respectively.[10-11] Furthermore, the pre-intercalation of metal cations (e.g., Na^+, Ca^{2+} and Mg^{2+}) or conducting polymers (e.g.,

polyaniline) into layered metal oxides, such as MoO_3, MnO_2 and V_2O_5, can expand their interlayer spacings, regulate their electronic properties and/or generate rich oxygen vacancies and thus could dramatically enhance their performance in rechargeable batteries, including Li-ion, Na-ion and Zinc-ion batteries.[12-19] Although the intercalation has been widely used as a promising strategy for structural engineering of layered materials, they mainly focused on the optimization of their performance in thermoelectric devices, electronic devices and rechargeable batteries. However, how the intercalation affects the performance of layered nanomaterials for biomedical applications, such as photothermal and catalytic therapy, still remain unexplored.

Nanomaterials with enzyme-mimicking oxidoreductase activities including peroxidase (POD), oxidase (OXD), and catalase (CAT), so-called "nanozymes", have been one of central topics in nanomedicine in the last decade since they can provide an ideal platform to realize highly efficient tumor diagnostic and/or therapeutic outcomes.[20-24] One of the major concerns for nanozymes is that their undesired off-target activity leads to unpredictable toxicity.[25,26] Hence, great effort has been devoted to the development of tumor microenvironment (TME)-responsive nanozymes that only exhibit catalytic reaction-based therapeutic effects, while minimum side effects in normal tissues.[27-29] Promisingly, recent studies have demonstrated that some nanozymes exhibit TME-responsive (e.g., H_2O_2- or pH-responsive) enzyme-mimicking catalytic activity and thus can achieve tumor-specific therapy since the microenvironment in tumors, such as the high H_2O_2 concentration and acidic pH value, is different from that of in normal tissues.[30-32] Among them, molybdenum oxide nanomaterials have been proven to be efficient nanozymes for tumor-specific catalytic therapy because of their low toxicity, variable oxidation states of Mo ions and excellent biodegradability.[34-38] For example, MoO_{3-x} nanourchins and Fe-MoO_v nanoparticles have been developed as efficient nanozymes for tumor-specific catalytic therapy and the structural engineering, including morphology tuning or defect engineering, has be proven to be essential to regulate their enzyme-mimicking catalytic activity.[36,37] However, the current reported molybdenum oxide-based nanozymes still suffer from the relatively low catalytic activity or need to introduce addtional active metal elements. Therefore, it is quite urgent to develop simple but effective strategies to prepare highly active redox nanozymes that are competitive to natural enzymes for catalytic therapy.

In this contribution, we report the intercalation as a promising strategy to activate the enzyme-mimicking catalytic activity of layered MoO_3 nanobelts, making it an efficient biodegradable nanozyme for tumor-specific photo-enhanced catalytic therapy. The hydrothermal-synthesized micrometer-long MoO_3 nanobelts are ball-milled and then co-intercalated with Na^+ and H_2O *via* aqueous solution intercalation to obtain the dark-blue co-intercalated MoO_3 nanobelts (denoted as NH-MoO_{3-x}) (Figure 1). Importantly, the co-intercalation not only can partially reduce the Mo^{6+} to Mo^{5+} and generate rich defects on the MoO_3 nanobelts, but also can boost its absorption in the near-infrared (NIR)-II region because of the bandgap narrowing. Thus, the NH-MoO_{3-x} nanobelts exhibit excellent enzyme-mimicking catalytic activity for generation of reactive oxygen species (ROS) including ·OH and $\cdot O_2^-$ in the TME in comparison with the inert MoO_3 nanobelts (Figure 1). Moreover, the enzyme-mimicking catalytic activity of NH-MoO_{3-x} nanobelts can be further enhanced by the photothermal effect under a 1064 nm laser irradiation. Thus, after modification with bovine serum albumin (BSA), the NH-MoO_{3-x}@BSA nanobelts exhibit remarkable tumor ablation when used as a nanozyme for the photo-driven tumor-specific catalytic therapy (Figure 1). Interestingly, the NH-MoO_{3-x}@BSA nanobelts are able to degrade rapidly and be excreted from the mice body, minimizing the *in vivo* toxicity for normal organs. This work provides a promising example on activating layered MoO_3 nanomaterials *via* intercalation as nanozymes for highly efficient tumor-specific catalytic therapy.

Results and Discussion

Single-crystalline MoO_3 nanobelts with micrometre lengths were prepared by a hydrothermal approach according to the previously reported method.[39] The X-ray diffraction (XRD) pattern of the MoO_3 nanobelts is shown in Figure 2a and all the peaks match well with the standard reference of the layered orthorhombic MoO_3 (α-MoO_3) (PDF 05-0508), confirming its crystal structure. As shown in the scanning electron microscope (SEM) image (Figure 2b), the prepared MoO_3 nanobelts have a length up to 5-10 μm and a width of hundreds of nanometres. The morphoogy and crystal structure of the MoO_3 nanobelts were further verified by transmission electron microscope (TEM) characgterization (Figure S1). In order to shorten its length, the micrometre-long MoO_3 nanobelts were grinded for 2 h *via* a dry ball milling process to obtain short MoO_3 nanobelts (denoted as MoO_3-BM). As shown Figure 2c, the SEM image shows that the MoO_3-BM nanobelts have a much shorter length, which is around 50-200 nm. The crystal structure of the MoO_3-BM nanobelts maintain well, which is evidenced by the scanning transmission electron microscope (STEM) and its corresponding atomic resolution STEM images (Figure S2). As shown in Figure S3, the XRD pattern of MoO_3-BM nanobelts matches well with the standard reference of the α-MoO_3 crystal (PDF 05-0508). All the aforementioned characterization results suggest that the balling milling mainly shortens the length of MoO_3 nanobelts.

The MoO_3-BM nanobelts were then intercalated with Na^+ and H_2O by reacting with sodium molybdate and sodium dithionite in aqueous solution to obtain NH-MoO_{3-x} nanobelts.[40] As shown in the XRD pattern, all the XRD peaks of the intercalated sample matches well with the simulated peaks based on the crystal structure of hydrated molybdenum bronze $[Na(H_2O)_2]_{0.25}MoO_3$ (Figure 2a).[40] This hydrated molybdenum bronze can be considered as the layered α-MoO_3 co-intercalated with Na^+ and H_2O. It is worth pointing out that the XRD peak corresponding to the (020) planes of the NH-MoO_{3-x} nanobelts shows an obvious shift to lower angle in comparison with that of the MoO_3 nanobelts. The peak position of (020) planes in the XRD pattern

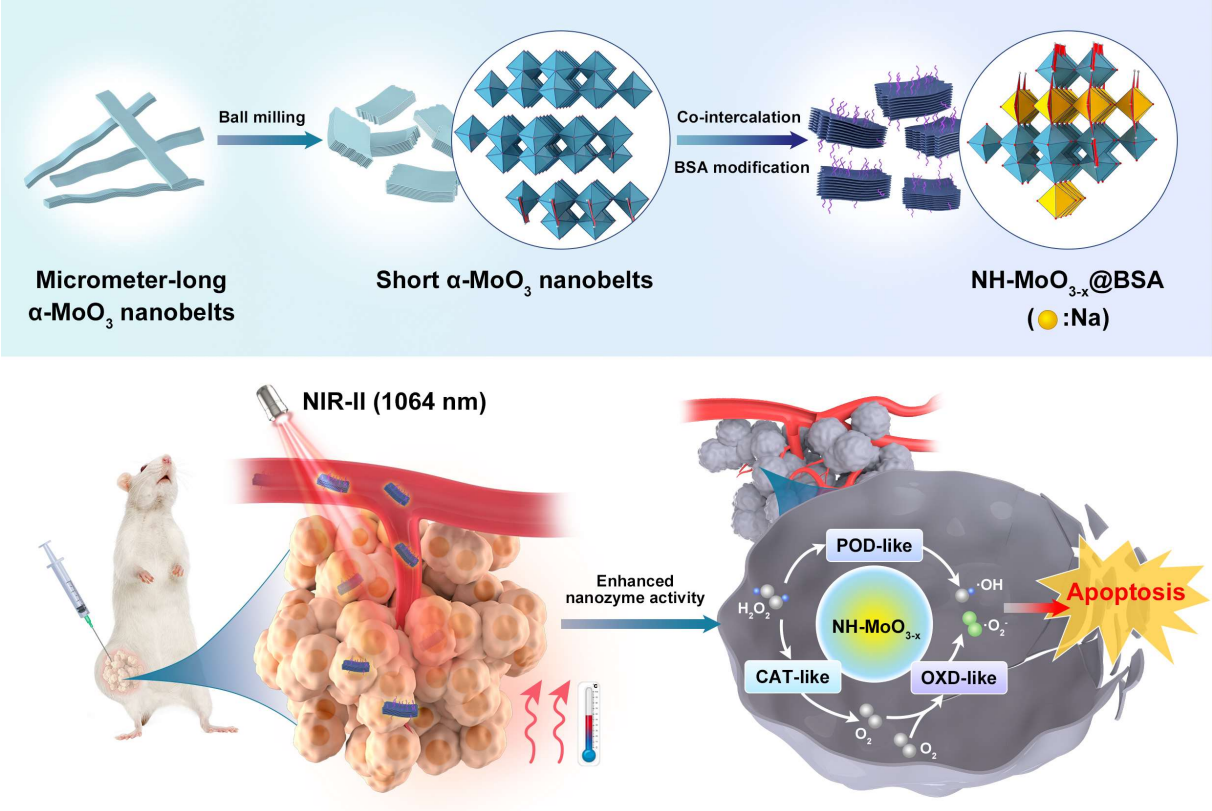

Figure 1. Scheme illustration of preparation of sodium-ion intercalated layered NH-MoO_{3-x} nanomaterial and its surface modification with BSA, and photo-enhanced catalytic therapy.

indicates the interlayer distancing of layered α-MoO_3. The obvious shift of this peak to lower angle suggests the expansion of the interlayer distancing of NH-MoO_{3-x} nanobelts induced by the co-intercalation with Na^+ and H_2O.

The SEM image clearly shows that the NH-MoO_{3-x} nanobelts have a uniform size of 100-300 nm (Figure 2d). The STEM image of the NH-MoO_{3-x} nanobelts (Figure 2e) displays a similar result with the SEM image. A continuous lattice fringe can be seen from the high-resolution STEM image (Figure 2f) of a typical NH-MoO_{3-x} nanobelt (inset in Figure 2f), indicating its single-crystalline characteristic. The measured lattice distance is ~0.38 nm, which is assignable to the (100) planes of the $[Na(H_2O)_2]_{0.25}MoO_3$ crystal. The Figure 2g shows the atomic resolution STEM image of MoO_3 nanobelt viewing from y-axis, suggesting that the MoO_3 nanobelt a layered structure and single-crystalline nature. The measured interlayer distancing is ~0.72 nm (Figure 2g), which is corresponding to the (020) planes of the layered α-MoO_3 crystal. Similarly, the atomic resolution STEM image of NH-MoO_3 nanobelts viewing from y-axis also displays its layered structure (Figure 2h). However, the measured interlayer distancing for the (020) planes is ~0.87 nm (Figure 2h), which is much larger than that of layered α-MoO_3 (i.e. 0.72 nm). Such results clearly prove the obvious expansion of the interlayer distancing of layered NH-MoO_{3-x} nanobelts as compared to the layered α-MoO_3 nanobelts, which is consistent with the XRD results. It is worth pointing out that not all the interlayer spacings are intercalated with Na^+ and H_2O since some parts of interlayer distancing still keep the same as the layered α-MoO_3 (Figure 2h). Meanwhile, some defects (indicating by arrows) can be also seen from the atomic resolution STEM image (Figure 2h), suggesting that the intercalation process also gives rise to some defects on the NH-MoO_{3-x} nanobelts.

X-ray photoelectron spectroscopy (XPS) was used to further characterize the structural changes of MoO_3 nanobelts caused by the co-intercalation. The high-resolution XPS Mo 3d of the MoO_3 and NH-MoO_{3-x} nanobelts are shown in Figure 3a. As shown in Figure 3a, the XPS Mo 3d spectrum of the MoO_3 nanobelts gives two peaks at 236.0 and 232.9 eV, which is attributed to the Mo^{6+} of MoO_3.[41,42] In contrast, the XPS Mo 3d spectrum of the NH-MoO_{3-x} presents two shoulder peaks at 234.7 and 231.6 eV, assignable to the Mo^{5+} in the NH-MoO_{3-x} nanobelts, in addition to the two main peaks at 236.0 and 232.9 eV.[41,42] Such a result indicates that the Mo atoms were partially reduced from Mo^{6+} to Mo^{5+} during the intercalation process. According to the deconvolution of the high-resolution XPS Mo 3d spectrum, the calculated perentage of Mo^{5+} is about 25.5% in the NH-MoO_3, which is consistent with the chemical formula of intercalated Na^+ (Figure 2c). Similarly, a new shoulder peak at 531.4 eV can be observed in the XPS O 1s spectrum of the NH-MoO_{3-x} nanobelts in addition to the main peak at 530.7 eV in comparison with the XPS O 1s spectrum of the MoO_3

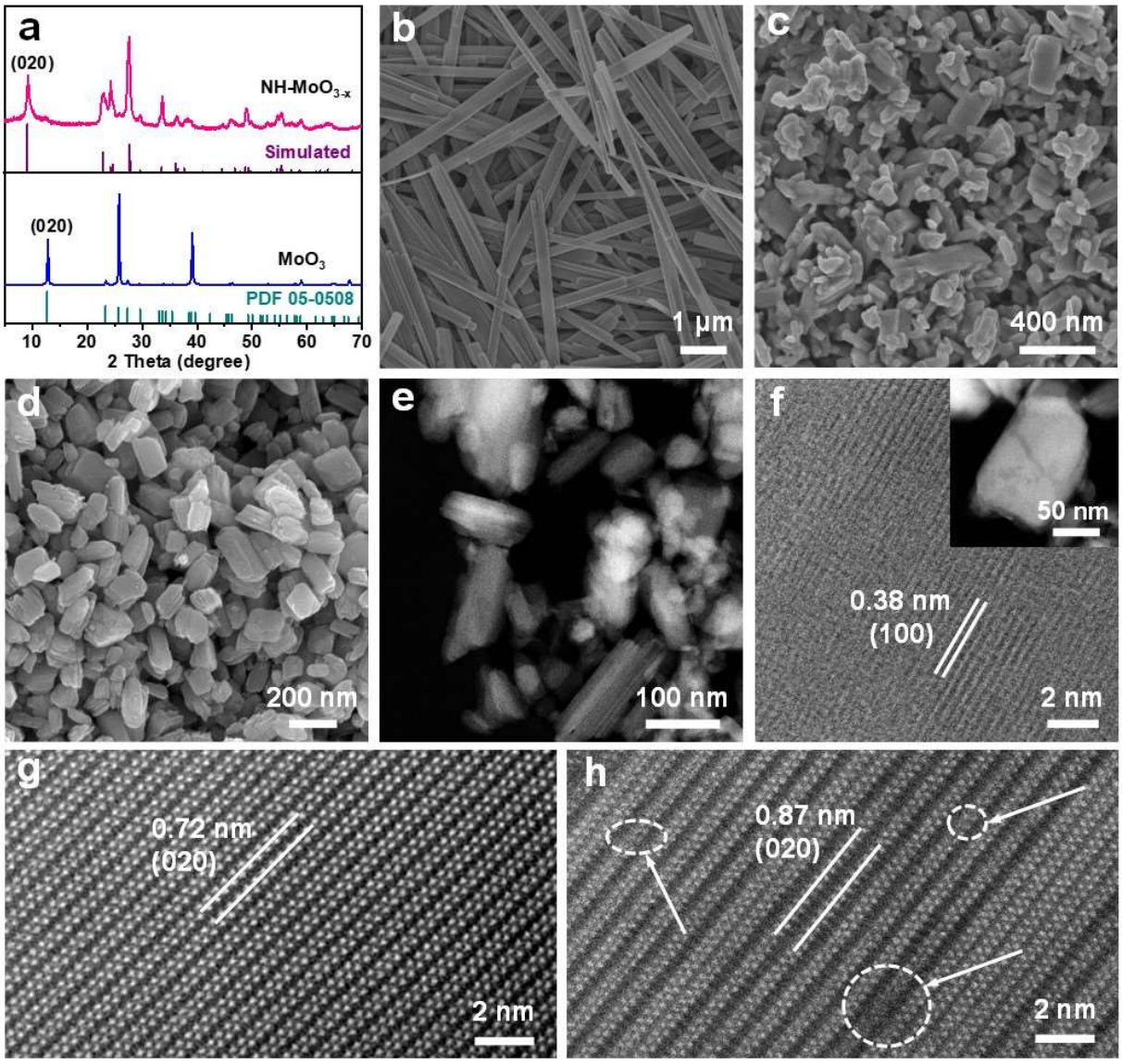

Figure 2. (a) XRD patterns of MoO_3 and NH-MoO_{3-x} with the corresponding references. SEM images of (b) MoO_3, (c) MoO_3-BM and (d) NH-MoO_{3-x}. (e, f) HAADF-STEM images of NH-MoO_{3-x}. Inset in (f) is HAADF-STEM image of NH-MoO_{3-x}. Atomic-resolution HAADF-STEM images of (g) MoO_3 and (h) NH-MoO_{3-x}. Arrows in (h) indicate the defect sites of the NH-MoO_{3-x}.

(Figure 3b), which might be due to oxygen vacancies caused by the partial reduction.[41,42] Importantly, in contract the non-detectable peak in XPS Na 1s spectrum of the MoO_3 nanobelts (Figure 3c), an obvious peak at 1071.8 eV corresponding to the Na^+ can be detected in XPS Na 1s spectrum of the NH-MoO_{3-x} nanobelts, confirming the presence of Na^+ in the NH-MoO_{3-x} nanobelts. The MoO_3 and NH-MoO_{3-x} nanobelts were also characterized by electron paramagnetic resonance (EPR) spectroscopy. As shown in Figure 3d, both of the MoO_3 and NH-MoO_{3-x} nanobelts display peaks at *g* values of 2.0 and 1.91, which are corresponding to the signals from oxygen vacancies and the Mo^{5+}, respectively.[43] It can be clearly observed that the NH-MoO_{3-x} nanobelts give much stronger intensity for both peaks than that of the MoO_3 nanobelts, suggesting that much more oxygen vacancies and Mo^{5+} ions in the NH-MoO_{3-x} nanobelts than those of the MoO_3 nanobelts.[43] The EPR results are consistent with analysis from other characterizations, including TEM and XPS. Furthermore, both of the MoO_3 and NH-MoO_{3-x} nanobelts were characterized by the Mo K-edge X-ray absorption near-edge structure (XANES) spectra. The radial atomic distribution around Mo atoms for both of the samples are evidenced by the Fourier transformed extended X-ray absorption fine structure (EXAFS) spectra (Figure 3e). Note that the NH-MoO_{3-x} nanobelts show slightly peak position shift and much lower peak intensity as compared to the MoO_3 nanobelts (Figure 3e). The much lower peak intensity suggests the significantly increased structure distortion and the peak position shift indicates the slightly changes on the bond lengths around Mo atoms, which can be attributed to the

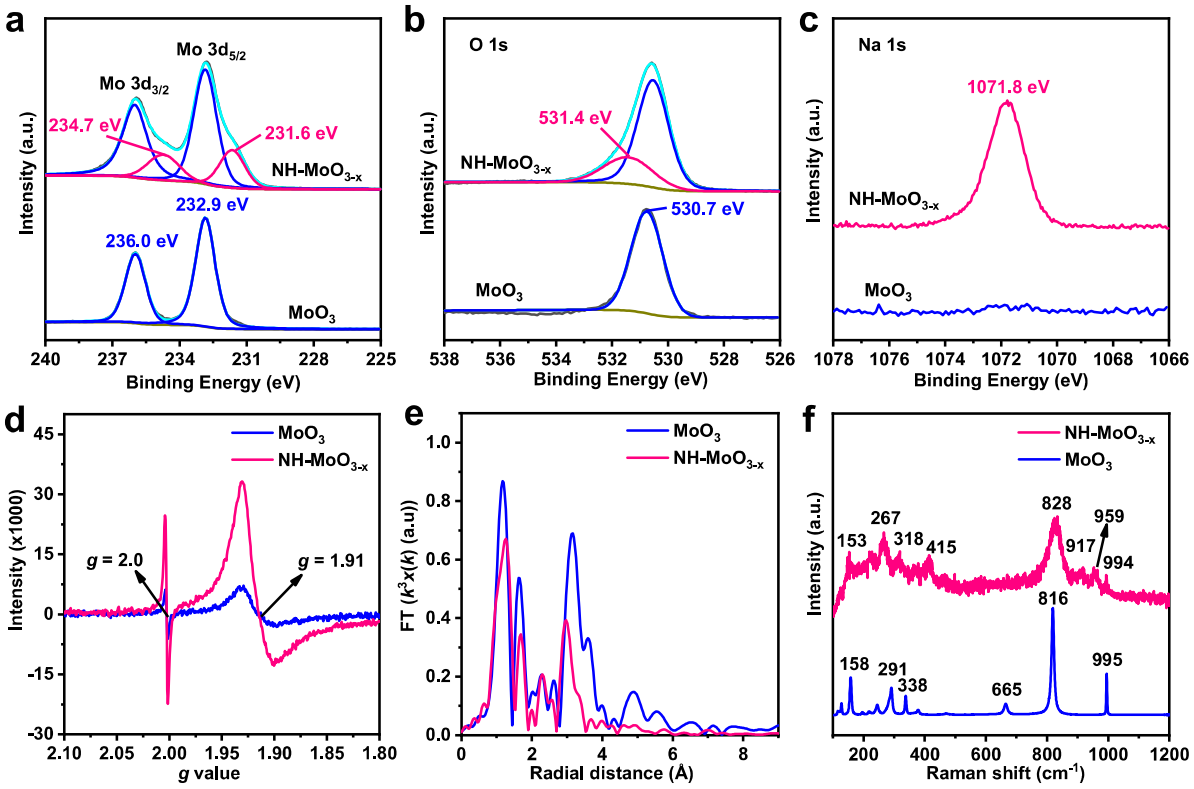

Figure 3. High resolution XPS (a) Mo 3d, (b) O 1s, and (c) Na 1s of MoO_3 and NH-MoO_{3-x}. (d) EPR spectra, (e) The Fourier transformed data of Mo K-edge EXAFS spectra of MoO_3 and NH-MoO_{3-x}. (f) The Raman spectra of MoO_3 and NH-MoO_{3-x}.

partial reduction of the Mo atoms and crystal structure induced by the intercalation, respectively.[44]

As shown in Figure 3f, the Raman spectrum of the NH-MoO_{3-x} nanobelts gives different characteristic peaks with much weaker intensity as compared to that of the MoO_3 nanobelts.[39] In addition, a few new characteristic peaks can be observed between 850-1000 cm^{-1}. The Raman spectrum change should be originated from the intercalation. Therefore, it was found that multiple structural changes can be achieved by the simple co-intercalation with Na^+ and H_2O into layered MoO_3 nanobelts, including partially reducing Mo^{6+} to Mo^{5+}, expanding the interlayer gaps, generating rich defects (e.g. oxygen vacancies) and changing crystal structure, to obtain short, interlayer gap-expanded and intercalated NH-MoO_{3-x} nanobelts.

The intercalation process can also give rise to a color change on the MoO_3 nanobelts from white to dark blue. As shown in Figure 4a, the photographs of powders and solutions of NH-MoO_{3-x} nanobelts show an obvious dark blue colour, distinctive from the white colour of the MoO_3 nanobelts. Therefore, the UV-vis-NIR absorption of the MoO_3, MoO_3-BM, and NH-MoO_{3-x} nanobelts are measured at the same concentration (100 ppm). The MoO_3 nanobelts exhibit weak absorption peaks in the range of 400 to 1300 nm and its absorption intensity gradually decreased could be attributed to light scattering induced by its micrometre-long length (Figure 4b). Note that the short MoO_3-BM nanobelts show negligible absorption intensity after 600 nm since the light scattering no longer exists because of the reduced size to hundreds of nanometres (Figure 4b). Interestingly, the absorption of NH-MoO_{3-x} nanobelts gradually increase along with the wavelength, resulting in strong absorption in the NIR-II window (Figure 4b), which is consistent with the UV-vis-NIR spectra calculated by density functional theory (DFT) (Figure 4c). In order to figure out the mechanism behind the absorption change, the electronic band structure and optical property were simulated by first principles DFT. We can find that the MoO_3 has a band gap of 2.592 eV, in which the valence band maximum (VBM) located at the high symmetry U point and the conduction band minimum (CBM) located at the X point (Figure 4d). In contrast, based on the calculation, the NH-MoO_{3-x} has a band gap of 1.793 eV (Figure 4e) which decreases 0.8 eV compared with the pristine MoO_3. It can be seen from the band structure that the conduction band of the NH-MoO_{3-x} also moves downward to the Fermi level as compared to the pristine MoO_3, since one Na atom was introduced in the MoO_3 crystal, which leads to a further narrowing of the band gap. Furthermore, as shown in the electronic energy band of NH-MoO_{3-x}, defect energy levels appear between the conduction band and the valence band from (Figure 4e). In this case, the defect energy levels could facilitate the electron transfer and the valence electrons could transit upward to the defect level first and then the conduction band. Hence, it is reasonable that the MoO_3 nanobelts have negligible absorption after 600 nm since it has a large band of ~2.592 eV. As for the NH-MoO_{3-x} nanobelts, the broad absorption band from visible to NIR region possibly is

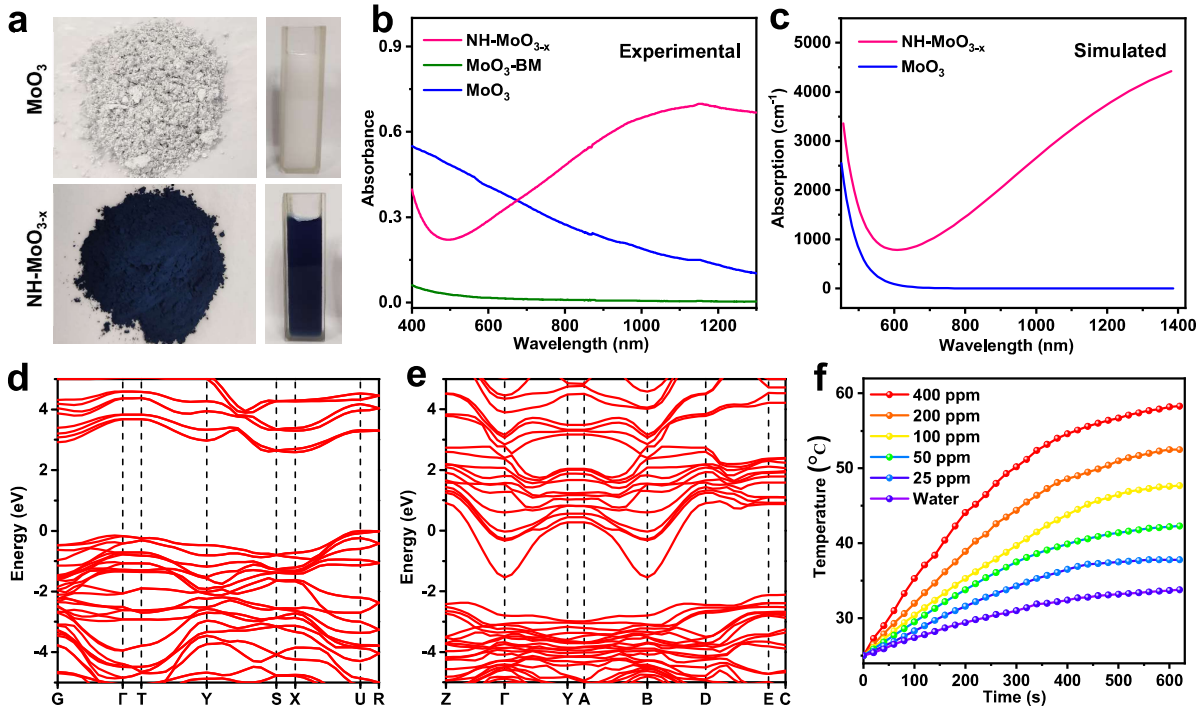

Figure 4. (a) Digital photographs in powder and solution, (b) UV-vis-NIR spectra of MoO_3 and NH-MoO_{3-x} nanobelts. (c) The simulated UV-vis-NIR spectra of MoO_3 and NH-MoO_{3-x}. Electronic energy band of (d) MoO_3 and (e) NH-MoO_{3-x}. (f) Heating curves of NH-MoO_{3-x}@BSA with various concentrations by irradiation using a 1064 nm NIR-II laser for 10 min at 1.0 W cm^{-2}.

caused its much smaller bandgap and defect energy level-enabled electron transition.

The UV-vis-NIR absorption intensity of the obtained NH-MoO_{3-x} nanobelts increased gradually from visible light to NIR region (especially in NIR-II region), which indicates that it has the potential to be used as a photothermal agent under a NIR laser radiation. As shown in the concentration-dependent absorption of NH-MoO_{3-x} nanobelts (Figure S4), its mass extinction coefficient at NIR-II (1064 nm) was calculated to be 6.7 L g^{-1} cm^{-1}. To promote the biocompatibility of inorganic nanomaterials, it is necessary to modify their surfaces with polymers (e.g., polyvinylpyrrolidone (PVP), polyethylene glycol (PEG) or Polyvinyl alcohol (PVA) or biological macromolecules (e.g., glutathione (GSH), hyaluronic acid (HA) or BSA). Therefore, a natural biological macromolecule, i.e., BSA, was used to modify the NH-MoO_{3-x} nanobelts to get the BSA-modified NH-MoO_3 nanobelts (NH-MoO_{3-x}@BSA). Then, the photothermal effect was studied by the continuous irradiation of DI water solution containing NH-MoO_{3-x}@BSA with various concentrations using a NIR-II laser (1064 nm) for 10 min at a power density of 1.0 W cm^{-2}. As shown in Figure 4f, the NH-MoO_{3-x}@BSA displays concentration-dependent heating effect under the NIR-II laser irradiation, and the water solution is heated from 25 °C to 58.3 °C by adjusting its concentration in contrast to the slight temperature changes (from 25 °C to 33.8 °C) for the pure DI water, indicating that NH-MoO_{3-x}@BSA could rapidly covert NIR light energy to the thermal energy. The solution of NH-MoO_{3-x}@BSA (200 ppm) was further irradiated with various laser power densities, and the heating curves displayed the amplitude of heating increased with the increase of laser power density (Figure S5a), demonstrating the laser power-dependent photothermal properties of NH-MoO_{3-x}@BSA. Moreover, the good photostability of NH-MoO_{3-x}@BSA was confirmed by the slight changes in its photothermal effect after five laser power on/off cycles (Figure S5b). The photothermal conversion efficiency of NH-MoO_{3-x}@BSA was calculated to be 24.27% based on its heating-cooling curve (Figure S5c,d), indicating that NH-MoO_{3-x}@BSA could effectively covert light energy to thermal energy.

The abundant oxygen vacancies, Mo^{5+}, and appropriate band gap of NH-MoO_{3-x} nanobelts makes it possible to be a nanozyme catalyst. After adding NH-MoO_{3-x}@BSA into a specific concentration of H_2O_2 solution, H_2O_2 was dramatically decomposed in a time-dependent manner under the neutral or weak acidic condition (Figure S6). The POD-like activity of NH-MoO_{3-x}@BSA was investigated by reducing H_2O_2 to ·OH that could be monitored by the traditional 3,3',5,5'-tetramethylbenzidine (TMB) substrate. NH-MoO_{3-x}@BSA presented significant POD-like activity (Figure 5a) in the HAc-NaAc buffer solution (pH 6.5), whereas almost no obvious catalytic activity was observed in the typical MoO_3 nanobelt (Figure S7) at the same conditions, which further proves that the POD-like activity of molybdenum oxide could be activated by Na^+ intercalation. When NH-MoO_{3-x}@BSA was irradiated by the 1064 nm NIR-II laser, its catalytic performance was improved to a certain extent in the buffer solution of pH 6.5 (Figure 5b), which might be due to the high temperature of the system to facilitate the nanozyme catalytic reaction. We further tested the

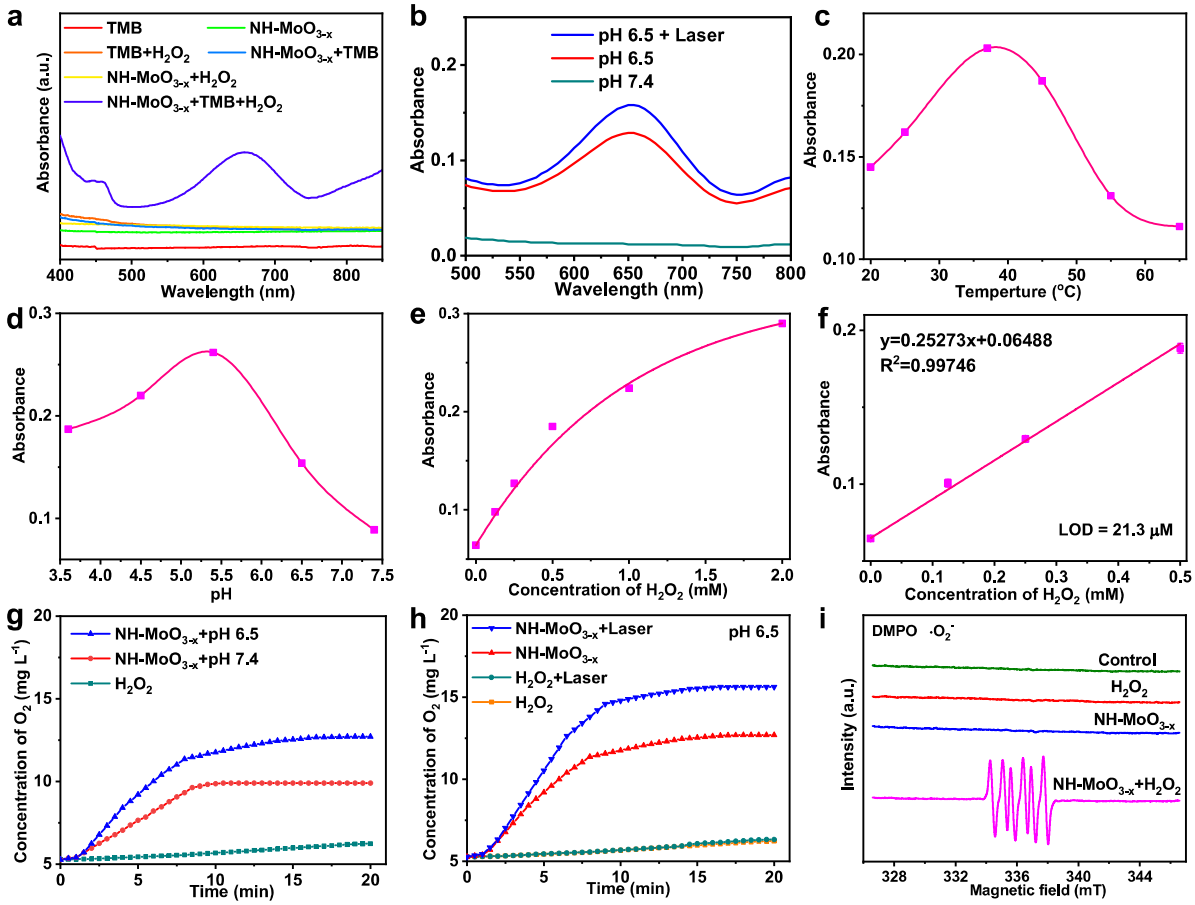

Figure 5. (a) UV-vis absorption spectra of oxTMB after different treatments (concentrations of NH-MoO_{3-x}: 50 μg mL^{-1}, H_2O_2: 1.0 mM, TMB: 1.0 mM, pH = 6.5). (b) NIR-II laser enhanced POD-like catalytic activity. (c) UV-vis absorption of oxTMB (1.0 mM) in the presence of H_2O_2 (1.0 mM) using NH-MoO_{3-x}@BSA (50μg mL^{-1}) as the POD mimic at pH = 5.0. (d) UV-vis absorption of blue oxTMB using NH-MoO_{3-x}@BSA as the POD mimic under the different pH values at 37 ℃. (e) The absorbance changes of oxTMB with various concentrations of H_2O_2 using TMB and NH-MoO_{3-x}@BSA as the substrate and POD mimic, respectively at 37 ℃. (f) The absorbance intensities of oxTMB at 650 nm versus the different concentrations of H_2O_2 (0-0.5 mM). (g) CAT-like catalytic activity of oxygen generation test results for NH-MoO_{3-x}@BSA in PBS with different pH values at 25 ℃ (concentration of NH-MoO_{3-x}: 50 μg mL^{-1}, H_2O_2: 1 mM). (h) NIR-II laser effect of CAT-like catalytic activity. (i) OXD-like catalytic activity testified by ESR spectra of NH-MoO_{3-x} in the presence of H_2O_2 using DMPO as the capture agent.

temperature-dependent POD-like activity of NH-MoO_{3-x}@BSA at different temperature (Figure 5c), and its optimal temperature ranged from 35 to 45 °C. Moreover, the pH-dependent POD-like activity of NH-MoO_{3-x}@BSA was also evaluated in different pH values at 37 °C, and its optimal pH ranged from 4.5 to 6.0 (Figure 5d and Figure S8a). The NH-MoO_{3-x}@BSA still maintained superior POD-like activity in the presence of low concentration H_2O_2 (Figure 5e and Figure S8b), and the UV-vis absorbance intensity at 652 nm (the characteristic peak for blue oxTMB) versus various concentrations (from 0 to 0.5 mM) of H_2O_2 exhibited a good linearity with the limit of detection as 21.3 μM (Figure 5f) that was lower than that of H_2O_2 in the tumor microenvironment (TME). According to the Lineweaver-Burk equation, the Michaelis-Menten constant (K_m) and maximal reaction velocity (V_{max}) were calculated to evaluate the catalytic ability of NH-MoO_{3-x}@BSA (Figure S9). The K_m / V_{max} value of NH-MoO_{3-x}@BSA was 2.41 mmol L^{-1} / 1.3×10^{-7} mol L^{-1} s^{-1} for H_2O_2 substrate with the concentration ranging from 0.5 to 10 mM, indicating the superior affinity of NH-MoO_{3-x}@BSA to H_2O_2 in comparison to that of natural horseradish peroxidase (HRP) (Table S1).[45]

Besides ·OH, O_2 can be produced by decomposing H_2O_2 under the catalysis of biological enzyme including catalase (CAT).[46] To investigate the CAT-like activity of NH-MoO_{3-x}@BSA, its oxygen production capacity was measured in the presence of H_2O_2 under different pH value buffer solutions. As shown in Figure 5g, the continuous oxygen can be detected after adding NH-MoO_{3-x}@BSA, and the yield of oxygen in weak acidic condition (mimicking TME) is obviously higher than that in neutral physiological environment, indicating NH-MoO_{3-x}@BSA can be used as a CAT-like nanozyme for decomposing intratumoral overexpressed H_2O_2 to produce O_2. Compared with NH-MoO_{3-x}@BSA, negligible CAT-like activity was observed for MoO_3 even under weak acidic condition (Figure S10a), demonstrating the CAT-like activity of molybdenum oxide could also be activated by the intercalation of Na^+. It is worth pointing

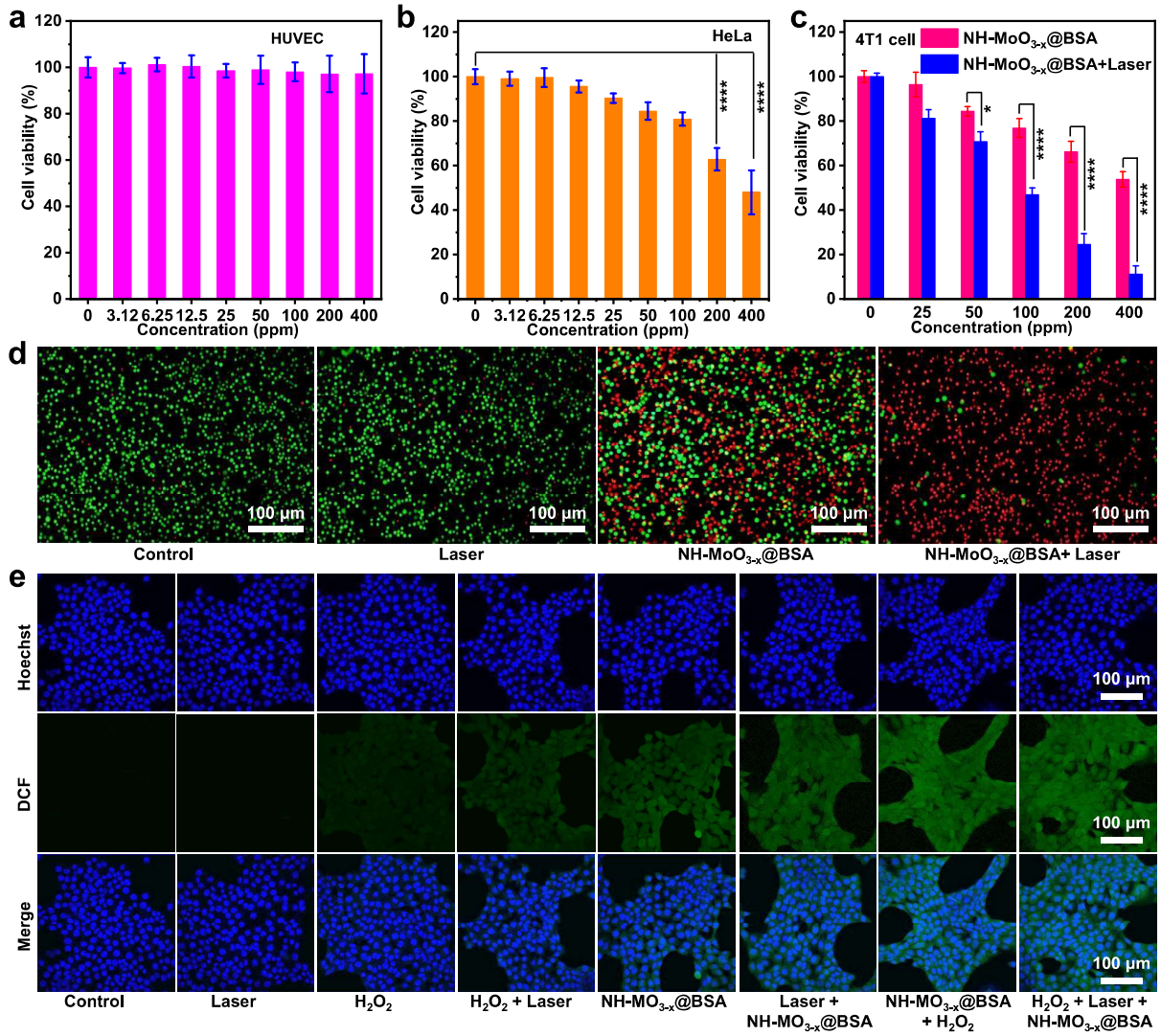

Figure 6. *In vitro* anti-tumor effect of NH-MoO_{3-x}@BSA. (a) Cell viabilities of (a) HUVEC and (b) HeLa cells with different concentrations of NH-MoO_{3-x}@BSA (Mean ± SD; n = 5 (analyzed using students' t-test, ****P < 0.0001)). (c) Cell viabilities of 4T1 cells with the treatment of various concentrations of NH-MoO_{3-x}@BSA in absence and presence of irradiation by a NIR-II laser (1064 nm, 0.8 W cm^{-2}) for 10 min (Mean ± SD; n = 5 (analyzed using students' t-test, *P < 0.1, ****P < 0.0001)). (d) Live/dead and (e) DCFH-DA/Hoechst staining of 4T1 cells cultured with different groups.

out that CAT-like performance of the NH-MoO_{3-x}@BSA could be improved under a NIR-II laser (1064 nm) irradiation (Figure 5h), contributing to the photothermal-enhanced catalytic effect. More importantly, the generated O_2 was further catalysed by NH-MoO_{3-x}@BSA to form superoxide free radical ($\cdot O_2^-$), which was proved by the electron spin resonance (ESR) assay. Only significant signal of $\cdot O_2^-$ was detected for the NH-MoO_{3-x}@BSA-catalyzed reaction (Figure 5i), indicating that NH-MoO_{3-x}@BSA had superior OXD-like activity to produce $\cdot O_2^-$ in comparison to MoO_3 nanobelts (Figure S10b).[47] All the aforementioned results proved that the NH-MoO_{3-x}@BSA nanobelts possess the multi-enzyme-like (POD, CAT, and OXD) property, and these integrated cascade catalytic reactions could effectively enhance the production of ROS ($\cdot OH$ and $\cdot O_2^-$) for catalytic therapy, which can be further accelerated by the photothermal effect under 1064 nm laser irradiation.

We believed that intercalation induced structural engineering, including partial reduction of Mo^{6+}, defect generation and interlayer spacing expansion, is attributed to the activation of the NH-MoO_{3-x} nanobelts. Previous studies have demonstrated that metal oxides with defects (e.g. oxygen vacancies) can effectively capture and activate H_2O_2 to generate $\cdot OH$ and O_2, thereby enhancing the catalytic properties of nanozymes.[37,48] In our NH-MoO_{3-x} nanobelts, the rich oxygen defects were formed after co-intercalating with Na^+ and H_2O into layered MoO_3 nanobelts (Figure 2h,3d), which can provide more active sites for the adsorption and activation of H_2O_2 to yield the more $\cdot OH$ and O_2. Subsequently, the adsorbed O_2 was reduced to $\cdot O_2^-$ through the charge transfer between Mo (V) and Mo (VI)[49] because of the partially reducing Mo^{6+} to Mo^{5+} (25.5 %) during the intercalation process. Meanwhile, the interlayer spacing of the NH-MoO_{3-x} nanobelts was also widened by the co-intercalation with Na^+ and H_2O, which can reduce its bandgap. The bandgap narrowing

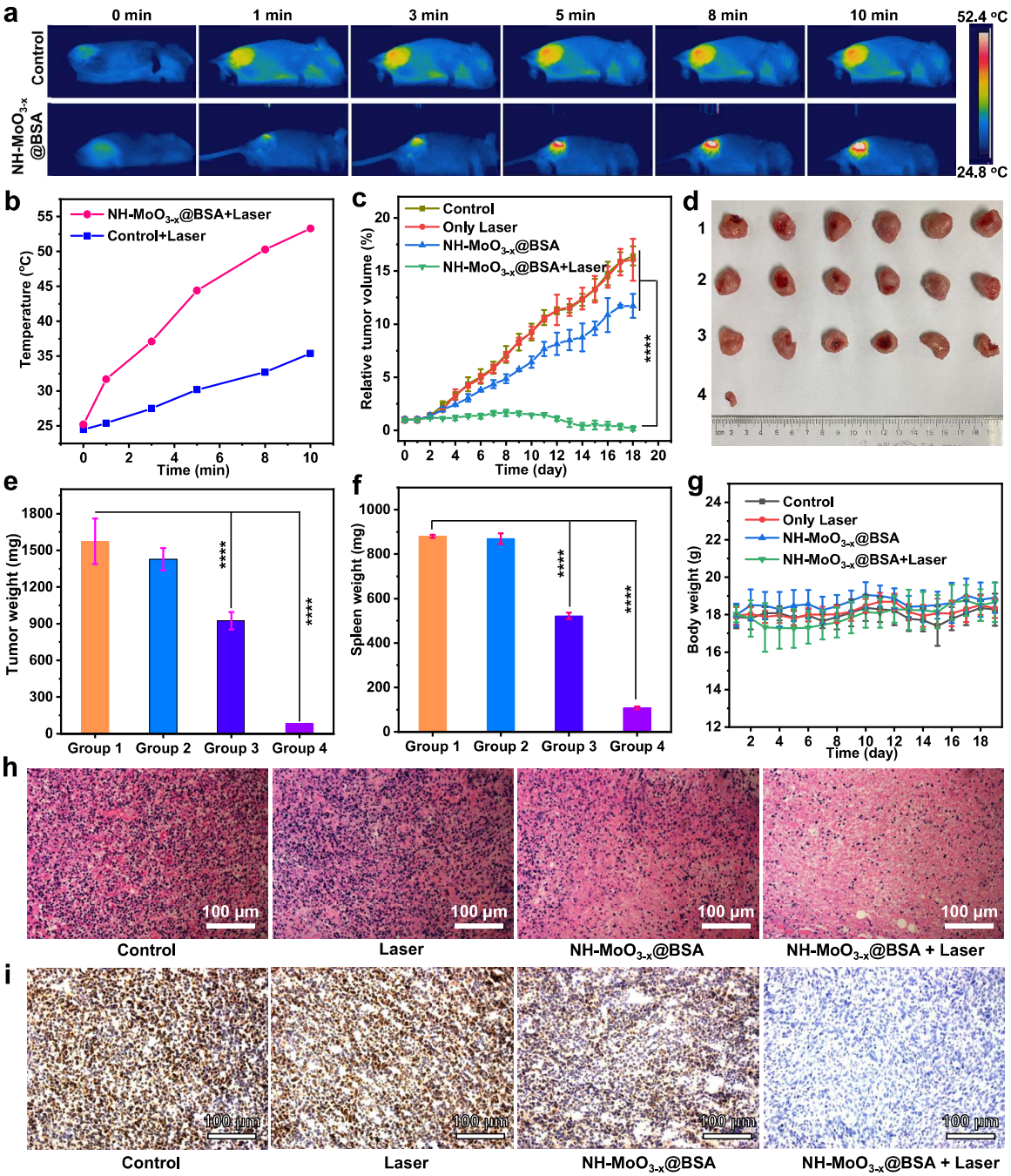

Figure 7. *In vivo* anti-tumor therapy of NH-MoO_{3-x}@BSA. (a) Thermal images and (b) the corresponding photothermal heating curves of control and NH-MoO_{3-x}@BSA groups under the irradiation of a 1064 nm laser (0.8 W cm^{-2}) for 10 min. (c) Relative tumor volume of the four groups during 19 days after treatment (Mean ± SD; n = 5 (two way ANOVA with a Bonferroni post hoc test, ****P < 0.0001)). (d) Photos of tumors in the four groups. (e) The weight of tumors and (f) spleens collected from different groups (Mean ± SD; n = 5 (analyzed using students' t-test, ****P < 0.0001)). Group 1: control, Group 2: only laser, Group 3: NH-MoO_{3-x}@BSA, Group 4: NH-MoO_{3-x}@BSA + Laser. (g) Body weight of the four groups during 19 days after treatment. (h) H&E and (i) Ki-67 staining of tumors harvested from the mice after different treatments at 19th day.

endows the NH-MoO_{3-x} nanobelts with strong absorption in the NIR-II window (Figure 4b,e), thereby enabling its good NIR-II photothermal properties. Temperature is one of the important factors affecting enzyme catalyzed reaction and the enzyme-catalyzed reaction will accelerate with the increase of temperature.[50] In our case, the increase of localized temperature induced photothermal effect will accelerate the rate of ROS generation and thus achieve highly efficient catalytic therapy. Therefore, layered MoO_3 nanobelts can be activated by intercalation, making it a highly active nanozyme for photo-enhanced catalytic therapy.

The *in vitro* cytotoxicity of NH-MoO_{3-x}@BSA was measured by the CCK-8 assay. Almost all the human umbilical vein endothelial cells (HUVEC) are still survive after treating with NH-

MoO_{3-x}@BSA for 24 h even at the high concentration of 400 ppm (Figure 6a), demonstrating that NH-MoO_{3-x}@BSA exhibited negligible cytotoxicity toward the normal cells with low H_2O_2 expression. As for the H_2O_2 high expressed cervical cancer cell line (HeLa) and mouse breast cancer cells (4T1), more than 50% of cells could be killed at a concentration of 400 ppm (Figure 6b,c), suggesting the enzyme-like catalytic activity of NH-MoO_{3-x}@BSA could be activated in the TME, which lead to the production of excess ROS and induce cell apoptosis. Meanwhile, we also investigated the photothermal effect of NH-MoO_3@BSA for 4T1 under the NIR-II laser irradiation (1064 nm, 0.8 W cm^{-2}) for 10 min. The cell viability was highly dependent on the concentration of NH-MoO_{3-x}@BSA after the PTT, and the cell survival rate was significantly lower than that of group without pre-irradiation by the NIR-II laser (Figure 6c), which was indicated PTT could enhance the catalytic activity of NH-MoO_3@BSA *in vitro*. Compared with hypoxic condition (Figure S11), the NH-MoO_{3-x} exhibits much higher cell inhibition rate under the normoxia, suggesting that it can be used for catalytic therapy *in vitro*. Moreover, the photo-enhanced enzyme catalysis using NH-MoO_{3-x}@BSA was further proved by co-staining with Calcein-AM and propidium iodide (PI). The living 4T1 cells (green colour) and dead cells (red colour) were distinguished by naked eye with the assistance of a confocal laser scanning microscopy (Figure 6d). Promisingly, most of the 4T1 cells were killed in the presence of NH-MoO_{3-x}@BSA (200 ppm) under the irradiation of a NIR-II laser (0.8 W cm^{-2}) for 10 min, and this cell mortality was much higher than that of group under the dark (Figure 6d), which might be due to the more reactive oxygen species (ROS) production stimulated by a NIR-II laser and the photothermal activity of NH-MoO_{3-x}@BSA. To further confirm the intracellular ROS producing ability of NH-MoO_{3-x}@BSA, 2′,7′-dichloro-fluorescein diacetate (DCFH-DA) and Hoechst as the classical fluorescent probes were used to monitor the intracellular ROS and nuclear localization, respectively. As shown in Figure 6e, the obvious green signal (DCF channel) was observed in the cells cultured with NH-MoO_{3-x}@BSA (200 ppm), which was demonstrated the generation of intracellular ROS. Compared to the NH-MoO_{3-x}@BSA group, the fluorescence intensity of cells in NH-MoO_{3-x}@BSA + H_2O_2 and NH-MoO_{3-x}@BSA + H_2O_2 + laser groups displayed a gradual increase, corroborating more ROS could be activated by the addition of external H_2O_2 and irradiation of NIR-II laser. These results indicated that NH-MoO_3@BSA could be used as a nanozyme to produce ROS in tumor cells through integrated cascade reaction, and kill cells.

The promising photo-enhanced enzymatic activities of NH-MoO_{3-x}@BSA on tumor cells make it have great potential in anti-tumor performance *in vivo*. 4T1 tumor-bearing BALB/c mice were assigned into four groups (six mice in each group): 1) control (PBS), 2) only laser (1064 nm, 0.8W cm^{-2}, 10 min), 3) NH-MoO_{3-x}@BSA (dosage: 5 mg/kg), 4) NH-MoO_{3-x}@BSA (dosage: 5 mg/kg) + laser (1064 nm, 0.8 W cm^{-2}, 10min). When the tumor volume is about 75 mm^3, the mice were intratumoral injected with PBS or NH-MoO_{3-x}@BSA solution (5 mg/kg). After 12 h, the tumor region was irradiated by the 1064 nm laser (0.8 W cm^{-2}) for 10 min, and its temperature changes were monitored by a IR thermal imager (Figure 7a). The temperature of tumor site in group 4 was dramatically increased to 53.3 °C after treating for 10 min (Figure 7b), while the temperature only increased to 35.4 °C for the group 2, demonstrating that NH-MoO_{3-x}@BSA possessed the good photothermal activity *in vivo*. In addition, the photo-enhanced catalytic cancer therapy of NH-MoO_{3-x}@BSA was explored by checking the changes of tumor volume, tumor weight, and body weight in different groups. The digital photos of mice in the four groups were taken at different period (Figure S12), and the tumors were effectively eliminated for the NH-MoO_{3-x}@BSA + laser group and the leaving black scar disappeared at 15th day. The tumor volumes and weight of mice in NH-MoO_{3-x}@BSA group were much lower than those of control and only laser groups (Figure 7c-e), indicating that NH-MoO_{3-x}@BSA had a certain enzyme inhibitory effect on tumors without laser. Upon irradiation by a 1064 nm laser, the tumor volumes and weight of mice decreased rapidly until almost disappeared in NH-MoO_{3-x}@BSA + laser group, proving that photothermal could enhance the anti-tumor properties of NH-MoO_{3-x}@BSA. The swelling of mouse spleen was significantly alleviated in group 4 (Figure 7f), which was further indicated the tumors of mice were effectively eliminated in NH-MoO_{3-x}@BSA + laser group. The body weight monitoring curves of mice in all the groups were very similar (Figure 7g), and no significant changes were observed, suggesting that NH-MoO_{3-x}@BSA had low toxicity *in vivo*. Hematoxylin and eosin (H&E) and Ki-67 staining of tumor tissues were also recorded and proved the effective suppressed cell proliferation treated with NH-MoO_{3-x}@BSA plus NIR-II laser group, while almost no obvious therapeutic effects were observed in the control, only laser and NH-MoO_{3-x}@BSA groups (Figure 7h and i).

To further evaluate the long-term biosafety of NH-MoO_{3-x}@BSA, its hemolysis experiment was first investigated. As shown in Figure S13, the hemolysis rate of NH-MoO_{3-x}@BSA was comparable to that of PBS control even at high concentration (300 ppm), proving it had good biosafety in blood. Secondly, blood samples of mice after different treatments at 19th day were utilized for routine blood test analysis (Figure S14) and blood biochemical assay (Figure S15). Most of the cell count parameters were normal in all four groups except for the abnormal increasing number of neutrophils (Figure S14a), monocytes (Figure S14b), lymphocytes (Figure S14c), and leukocytes (Figure S14d) in group 1, 2, and 3, which was probably attributed to the inflammation, bacterial or viral infections caused by the tumor. However, the above abnormal parameters returned to normal values after eliminating the tumors in the group 4. Importantly, the amount of alkaline phosphatase (ALP) in the mouse blood was also significantly improved after the treatment of NH-MoO_{3-x}@BSA + laser (Figure S15f). Thirdly, the tissue and organ sections of mice for H&E staining and the distribution of molybdenum ions were investigated in detail. No obvious damage was observed in the NH-MoO_{3-x}@BSA + laser group in comparison with the control group (Figure S16). More importantly, inductively coupled plasma mass spectrometry (ICP-MS) measurement (Figure S17)

indicated that the accumulation of molybdenum ions in all organs of mice in NH-MoO_{3-x}@BSA + laser group was extremely low, which was close to that of the PBS control group, demonstrating the NH-MoO_{3-x}@BSA could be degraded in mice and excreted from the body with negligible biotoxicity *in vivo*.

Conclusion

In summary, we have reported the activation of layered MoO_3 nanobelts through aqueous Na^+/H_2O co-intercalation used as highly active nanozymes for photo-enhanced catalytic therapy. Our results have shown that the intercalation can endow the inert MoO_3 nanobelts with excellent enzyme-mimicking catalytic activity towards the enhanced generation of vast ROS under mimic TME. Meanwhile, the co-intercalation can also activate the absorption of layered MoO_3 nanobelts in the NIR region, thus enabling its good photothermal effect under a NIR-II laser irradiation. Importantly, the enzyme-mimicking catalytic activity of the NH-MoO_{3-x} nanobelts can be further enhanced by the NIR-laser-induced photothermal effect. Both the *in vitro* and *in vivo* have proven that the NH-MoO_3 nanobelts could serve as a highly active nanozyme for selectively killing cancer cells. Importantly, the NH-MoO_{3-x}@BSA nanobelts presented excellent biodegradability and could be easy to be excreted from normal organs with negligible *in vivo* toxicity. Our study has revealed that aqueous intercalation is a simple and effective strategy to activate layered MoO_3 for highly efficient photo-enhanced catalytic therapy. We believe that this intercalation strategy could also be an effective way to activate/optimize layered metal oxides for other biomedical applications, such as chemodynamic, photodynamic and sonodynamic therapy. In addition, such an intercalation strategy is expected to be also a powerful approach for activating/tuning other layered materials, such as metal chalcogenides, Mxenes, and layered double hydroxides, as highly active nanozymes towards catalytic therapy.

Acknowledgements

Z.Z. thanks the funding support from National Natural Science Foundation of China (52102348), Tackle Key Problem of Science and Technology Project of Henan Province (212102310073) and the funding support from China Postdoctoral Science Foundation (2021M701113). W.Y. thanks the funding support from National Natural Science Foundation of China (U1932112, 22175182, 51772293), Beijing Natural Science Foundation (2202064). C.T. thanks the funding support from the Start-Up Grant (9610495) and Grants (9680297, 7020013) from City University of Hong Kong and the National Natural Science Foundation of China (22005259, 52122002).

Keywords: layered MoO_3 • intercalation • nanozymes • tumor-specific • catalytic therapy

[1] V. Nicolosi, M. Chhowalla, M. G. Kanatzidis, M. S. Strano, J. N. Coleman, *Science* **2013**, *340*, 1226419.
[2] P. Ajayan, P. Kim, K. Banerjee, *Phys. Today* **2016**, *69*, 38.
[3] D. L. Duong, S. J. Yun, Y. H. Lee, *ACS Nano* **2017**, *11*, 11803-11830.
[4] J. Zhou, Z. Lin, H. Ren, X. Duan, I. Shakir, Y. Huang, X. Duan, *Adv. Mater.* **2021**, *33*, 2004557.
[5] X. Zhao, P. Song, C. Wang, A. C. Riis-Jensen, W. Fu, Y. Deng, D. Wan, L. Kang, S. Ning, J. Dan, T. Venkatesan, Z. Liu, W. Zhou, K. S. Thygesen, X. Luo, S. J. Pennycook, K. P. Loh, *Nature* **2020**, *581*, 171-177.
[6] M. S. Stark, K. L. Kuntz, S. J. Martens, S. C. Warren, *Adv. Mater.* **2019**, *31*, 1808213.
[7] J. Wan, S. D. Lacey, J. Dai, W. Bao, M. S. Fuhrer, L. Hu, *Chem. Soc. Rev.* **2016**, *45*, 6742-6765.
[8] H. Wang, Z. Lu, S. Xu, D. Kong, J. J Cha, G. Zheng, P.-C. Hsu, K. Yan, D. Bradshaw, F. B Prinz, Y. Cui, *Proc. Natl. Acad. Sci. U.S.A.* **2013**, *110*,19701-19706.
[9] Y. Gong, H. Yuan, C.-L. Wu, P. Tang, S.-Z. Yang, A. Yang, G. Li, B. Liu, J. van de Groep, M. L. Brongersma, M. F. Chisholm, S.-C. Zhang, W. Zhou, Y. Cui, *Nat. Nanotechnol.* **2018**, *13*, 294-299.
[10] C. Wan, X. Gu, F. Dang, T. Itoh, Y. Wang, H. Sasaki, M. Kondo, K. Koga, K. Yabuki, G. J. Snyder, *Nat. Mater.* **2015**, *14*, 622-627.
[11] C. Wang, Q. He, U. Halim, Y. Liu, E. Zhu, Z. Lin, H. Xiao, X. Duan, Z. Feng, R. Cheng, N. O Weiss, G. Ye, Y.-C. Huang, H. Wu, H.-C. Cheng, I. Shakir, L. Liao, X. Chen, W. A Goddard III, Y. Huang, X. Duan, *Nature* **2018**, *555*, 231-236.
[12] C. Xia, J. Guo, P. Li, X. Zhang, H. N. Alshareef, *Angew. Chem. Int. Ed.* **2018**, *57*, 3943-3948; *Angew. Chem.* **2018**, *130*, 4007-4012.
[13] F. Ming, H. Liang, Y. Lei, S. Kandambeth, M. Eddaoudi, H. N. Alshareef, *ACS Energy Lett.* **2018**, *3*, 2602-2609.
[14] M. Yan, P. He, Y. Chen, S. Wang, Q. Wei, K. Zhao, X. Xu, Q. An, Y. Shuang, Y. Shao, K. T. Mueller, L. Mai, J. Liu, J. Yang, *Adv. Mater.* **2018**, *30*, 1703725.
[15] D. Wang, L. Wang, G. Liang, H. Li, Z. Liu, Z. Tang, J. Liang, C. Zhi, *ACS Nano* **2019**, *13*, 10643-10652.
[16] Y. Yang, Y. Tang, S. Liang, Z. Wu, G. Fang, X. Cao, C. Wang, T. Lin, A. Pan, J. Zhou, *Nano Energy* **2019**, *61*, 617-625.
[17] J. Huang, Z. Wang, M. Hou, X. Dong, Y. Liu, Y. Wang, Y. Xia, *Nat. Commun.* **2018**, *9*, 2906.
[18] S. Liu, H. Zhu, B. Zhang, G. Li, H. Zhu, Y. Ren, H. Geng, Y. Yang, Q. Liu, C. C. Li, *Adv. Mater.* **2020**, *32*, 2001113.
[19] J. Zhao, Z. Xu, Z. Zhou, S. Xi, Y. Xia, Q. Zhang, L. Huang, L. Mei, Y. Jiang, J. Gao, Z. Zeng, C. Tan, *ACS Nano* **2021**, *15*, 10597-10608.
[20] M. Huo, L. Wang, Y. Chen, J. Shi, *Nat. Commun.* **2017**, *8*, 357.
[21] Z. Wang, Y. Zhang, E. Ju, Z. Liu, F. Cao, Z. Chen, J. Ren, X. Qu, *Nat. Commun.* **2018**, *9*, 3334.
[22] K. Fan, J. Xi, L. Fan, P. Wang, C. Zhu, Y. Tang, X. Xu, M. Liang, B. Jiang, X. Yan, L. Gao, *Nat. Commun.* **2018**, *9*, 1440.
[23] H. Zhang, X. Pan, Q. Wu, J. Guo, C. Wang, H. Liu, *Exploration* **2021**, *1*, 20210010.
[24] F. Cao, L. Zhang, H. Wang, Y. You, Y. Wang, N. Gao, J. Ren, X. Qu, *Angew. Chem. Int. Ed.* **2019**, *58*, 16236-16242; *Angew. Chem.* **2019**, *131*, 16382-16388.
[25] Z. Cheng, A. Al Zaki, J. Z. Hui, V. R. Muzykantov, A. Tsourkas, *Science* **2012**, *338*, 903-910.
[26] M. W. Tibbitt, J. E. Dahlman, R. Langer, *J. Am. Chem. Soc.* **2016**, *138*, 704-717.
[27] H. Wei, E. Wang, *Chem. Soc. Rev.* **2013**, *42*, 6060-6093.
[28] Y. Huang, J. Ren, X. Qu, *Chem. Rev.* **2019**, *119*, 4357-4412.
[29] Z. Zhou, G. Roelfes, *Nat. Catal.* **2020**, *3*, 289-294.
[30] J. Lu, J. Sun, F. Li, J. Wang, J. Liu, D. Kim, C. Fan, T. Hyeon, D. Ling, *J. Am. Chem. Soc.* **2018**, *140*, 10071-10074.
[31] S. Li, L. Shang, B. Xu, S. Wang, K. Gu, Q. Wu, Y. Sun, Q. Zhang, H. Yang, F. Zhang, L. Gu, T. Zhang, H. Liu, *Angew. Chem. Int. Ed.* **2019**, *58*, 12624-12631; *Angew. Chem.* **2019**, *131*, 12754-12761.
[32] Y. Zhu, W. Wang, J. Cheng, Y. Qu, Y. Dai, M. Liu, J. Yu, C. Wang, H. Wang, S. Wang, C. Zhao, Y. Wu, Y. Liu, *Angew. Chem. Int. Ed.* **2021**, *60*, 9480-9488; *Angew. Chem.* **2021**, *133*, 9566-9574.
[33] L. Teng, X. Han, Y. Liu, C. Lu, B. Yin, S. Huan, X. Yin, X.-B. Zhang, G. Song, *Angew. Chem. Int. Ed.* **2021**, DOI: 10.1002/anie.202110427.

[34] Y. Zu, H. Yao, Y. Wang, L. Yan, Z. Gu, C. Chen, L. Gao, W. Yin, *View* **2021**, *2*, 20200188.
[35] Y. Zhang, D. Li, J. Tan, Z. Chang, X. Liu, W. Ma, Y. Xu, *Small* **2021**, *17*, 2005739.
[36] B. Yu, W. Wang, W. Sun, C. Jiang, L. Lu, *J. Am. Chem. Soc.* **2021**, *143*, 8855-8865.
[37] X. Hu, F. Li, F. Xia, X. Guo, N. Wang, L. Liang, B. Yang, K. Fan, X. Yan, D. Ling, *J. Am. Chem. Soc.* **2020**, *142*, 1636-1644.
[38] Y. Zhang, D. Li, J. Tan, Z. Chang, X. Liu, W. Ma, Y. Xu, *Small* **2020**, *17*, 2005739.
[39] X. Yang, H. Tang, R. Zhang, H. Song, K. Cao, *Cryst. Res. Technol.* **2011**, *46*, 409.
[40] D. M. Thomas, E. M. McCarron III, *Mat. Res. Bull.* **1986**, *21*, 945-960.
[41] J. S´wiatowska-Mrowiecka, S. de Diesbach, V. Maurice, S. Zanna, L. Klein, E. Briand, I. Vickridge, P. Marcus, *J. Phys. Chem. C* **2008**, *112*, 11050-11058.
[42] Z. Zhou, X. Wang, H. Zhang, H. Huang, L. Sun, L. Ma, Y. Du, C. Pei, Q. Zhang, H. Li, L. Ma, L. Gu, Z. Liu, L. Cheng, C. Tan, *Small* **2021**, *17*, 2007486.
[43] R. Xiong, J. Shi, Q. Xiao, W. Tang, H. Liu, D. Tian, *J. Mater. Sci.* **2001**, *6*, 5511-5514.
[44] Z. Sun, Q. Liu, T. Yao, W. Yan, S. Wei, *Sci. China Mater.* **2015**, *58*, 313-341.
[45] L. Gao, J. Zhuang, L. Nie, J. Zhang, Y. Zhang, N. Gu, T. Wang, J. Feng, D. Yang, S. Perrett, X. Yan, *Nat. Nanotechnol.* **2007**, *2*, 577-583.
[46] P. George, *Nature* **1947**, *160*, 41-43.
[47] L. Gao, R. Liu, F. Gao, Y. Wang, X. Jiang, X. Gao, *ACS Nano* **2014**, *8*, 7260-7271.
[48] X. Wang, X. Zhong, L. Bai, J. Xu, F. Gong, Z. Dong, Z. Yang, Z. Zeng, Z. Liu, L. Cheng, *J. Am. Chem. Soc.* **2020**, *142*, 6527-6537.
[49] Y. Kuwahara, Y. Yoshimura, K. Haematsu, H. Yamashita, *J. Am. Chem. Soc.* **2018**, *140*, 9203-9210.
[50] S. Dong, Y. Dong, T. Jia, S. Liu, J. Liu, D. Yang, F. He, S. Gai, P. Yang, J. Lin, *Adv. Mater.* **2020**, *32*, 2002439.

10.1002/anie.202115939

WILEY-VCH

Entry for the Table of Contents

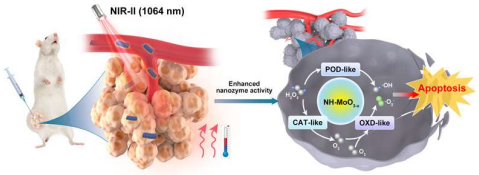

The aqueous intercalation is proposed here as a promising strategy to activate the enzyme-mimicking catalytic activity of layered MoO_3 nanobelts for generation of reactive oxygen species including ·OH and $·O_2^-$ in tumor microenvironment, making it an efficient biodegradable nanozyme for tumor-specific photo-enhanced catalytic therapy.